The formation of discontinuous gradient regimes during crack initiation in high strength steels under very high cycle fatigue

Chengqi Sun[a,b], Qingyuan Song[a,b], Lingling Zhou[a], Jialong Liu[c], Yao Wang[a,d], Xiaolei Wu[a,b], Yujie Wei[a,b,*]

[a] State Key Laboratory of Nonlinear Mechanics, Institute of Mechanics, Chinese Academy of Sciences, Beijing 100190, China
[b] School of Engineering Sciences, University of Chinese Academy of Sciences, Beijing 100049, China
[c] Institute of Geology and Geophysics, Chinese Academy of Sciences, Beijing 100029, China
[d] Key Laboratory of Vehicle Advanced Manufacturing, Measuring and Control Technology, Beijing Jiaotong University, Beijing 100044, China

ARTICLE INFO

ABSTRACT

While fatigue is ubiquitous and is responsible for a large proportion of failure in engineering structures, we understand little regarding the mechanism of crack initiation and early-stage crack growth especially for very high cycle fatigue (VHCF) behavior. We identified in this report the microstructural evolution during interior crack initiation and early growth in a martensitic stainless steel in VHCF regime by constant and variable amplitude loading method. We observed in the post-mortem samples after VHCF a discontinuous gradient layer composed of ultrafine grains and coarse grains in the fractured surfaces using both electron backscatter diffraction (EBSD) and transmission electron microscopy (TEM). The gradient ultrafine grains are resulted from excessive cyclic plastic deformation in the vicinity of the crack origin or crack tip, which promotes the formation of crack initiation. The equivalent crack growth rate in FGA (fine granular area) is also estimated based on the "tree ring" patterns under variable amplitude loading, which is in the magnitude of 10^{-12}–10^{-11} m/cyc.

1. Introduction

Fatigue failure is commonly seen in mechanical components subjected to cyclic loadings. Regardless the large variability in the loading history of materials in real engineering practice, researchers categorized laboratory fatigue tests into low cycle fatigue, high cycle fatigue (HCF), and very high cycle fatigue (VHCF) [1–9]. The latter is particularly referred to fatigue failure beyond 10^7 loading cycles [10–13]. VHCF becomes a new regime of fatigue research for the everlasting demand of faster speed and longer duration. In the classical stress - reversal number (S-N) curves of most engineering materials in HCF regime, there exists a stress plateau below which the material may presumably have infinite life-time. The idealized infinite life has been challenged in engineering practice, which has been boosting the research on VHCF. It has been now established that non-metallic inclusions in the interior of materials, even at lower stress levels, may lead to VHCF [14–19]. The interior crack-induced failure at low stress levels is usually featured by a 'fish-eye' pattern [20]. Inside the fish-eye, it has been identified that there exists a fine granular area (FGA) which is particularly rough [21]. Although there are different names associated with this regime [8,22], there is a consensus regarding the formation of FGA.

The formation of FGA is intriguing as it is closely related to the accuracy of fatigue life prediction. However, the very small size of FGA and forming in the interior of the specimen [20] make a direct observation very difficult to explore the crack initiation formation mechanism of FGA and measure the evolvement process of crack initiation in FGA. Shiozawa et al. [23] proposed that the formation of FGA was due to decohesion of spherical carbides from the matrix in the vicinity of an inclusion. The coalesced crack along the boundary between the spherical carbides and the matrix resulted in the FGA region. Nakamura et al. [24] and Ogawa et al. [25] proposed that FGA was formed by long term repeating compressive loading over about 10^7 cycles after fatigue crack was generated, other than the crack growth stage. Grad et al. [26] and Sakai et al. [27] suggested a scenario where the FGA was formed in three consequential stages: (i) formation of fine granular layer, (ii) nucleation of microcracks, and (iii) coalescence of microcracks and complete formation of an FGA.

Regardless the tremendous progress in understanding the development of FGA, the exact mechanism associated with the formation of FGA and its implication with fatigue remains controversial. In this work, we used both constant and variable amplitude loadings to
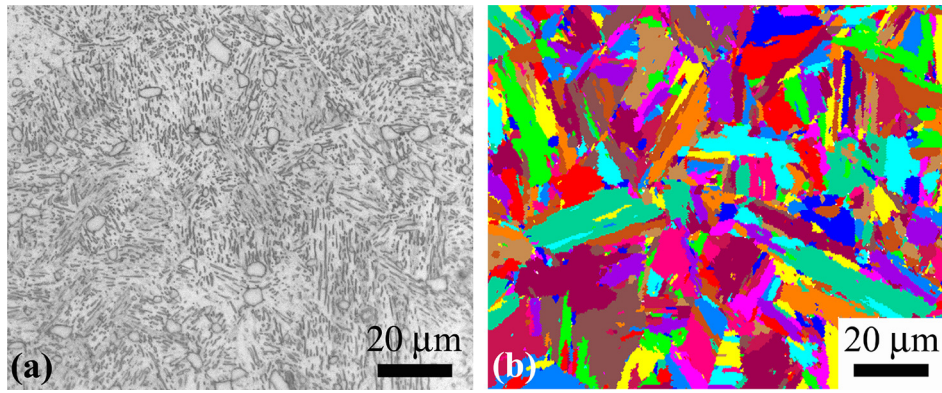
Fig. 1. (a) and (b) Microstructure pictures of the tested martensitic stainless steel.
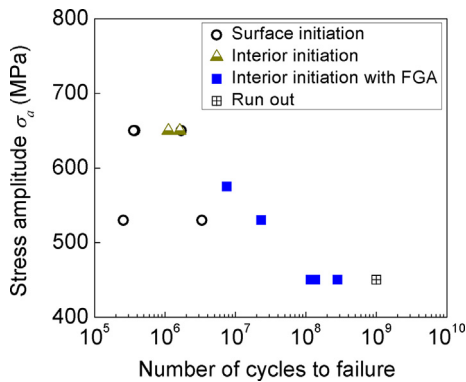

Fig. 2. S-N data of the samples under constant stress amplitude.

investigate and capture the mechanism of crack initiation and early-stage growth in VHCF regime in a martensitic stainless steel, and reveal the existence of a discontinuous gradient layer in the fracture surfaces of fatigued samples using both transmission electron microscopy (TEM) and electron backscatter diffraction (EBSD). The formation mechanism of gradient layer is also proposed.

2. Materials and methods

2.1. Materials

The material used is a martensitic stainless steel 0cr17ni4cu4nb (AISI630) with chemical compositions 0.047 C, 15.58 Cr, 3.65 Ni, 3.11 Cu, 0.74 Mn, 0.18 Nb, 0.16 Mo and balanced Fe in weight percent. Specimens were first heated at 1050 °C for 60 min and cooled in air, then heated at 850 °C for 3 h and oil-quenched, and finally tempered for 4 h at 470 °C with air-cooling. The tensile test was conducted on two cylindrical specimens with diameter of 5 mm and gauge length of
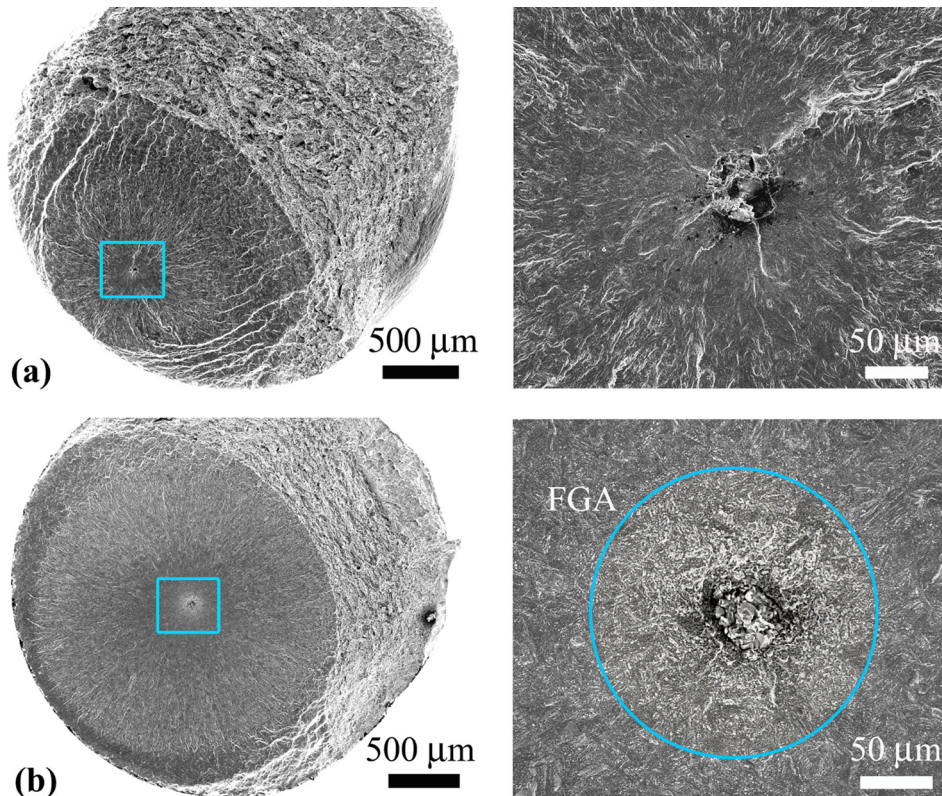

Fig. 3. SEM images of fracture surface of specimens under constant stress amplitude. (a) $\sigma_a = 650$ MPa, $N_f = 1.11 \times 10^6$; (b) $\sigma_a = 450$ MPa, $N_f = 2.8 \times 10^8$.
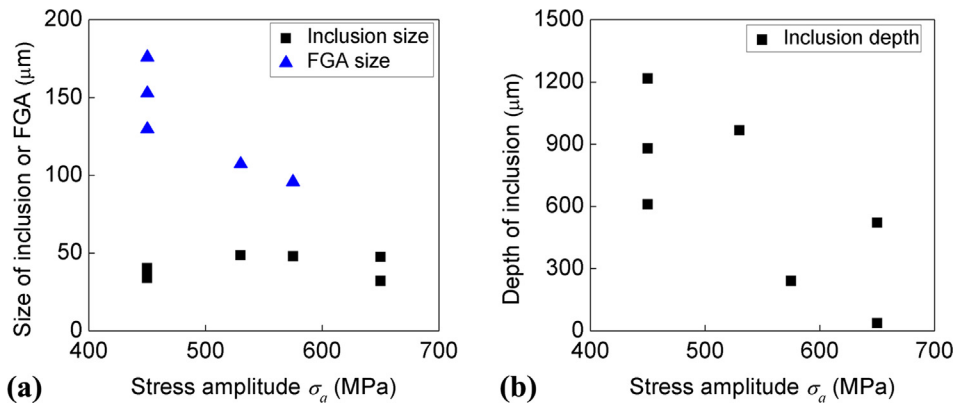
Fig. 4. (a) Variation of inclusion size and FGA size with stress amplitude; (b) Variation of inclusion depth with stress amplitude.
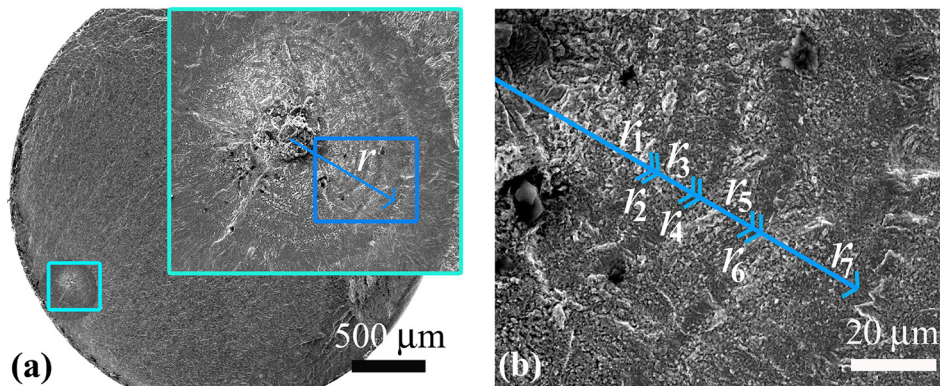

Fig. 5. (a) and (b) SEM images of fracture surface for the specimen failed at a total fatigue life of 8.576×10^7 ($\sigma_a^H = 650$ MPa, $n_H = 4 \times 10^3$, $\sigma_a^L = 430$ MPa, $n_L = 3 \times 10^6$) with "tree ring" pattern under variable amplitude loading.
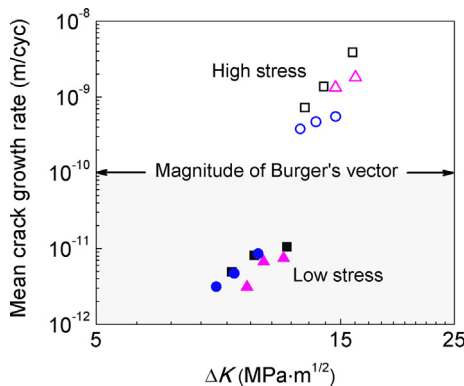

Fig. 6. Mean crack growth rate versus stress intensity factor at different stress amplitudes.

30 mm using the servohydraulic test system. The yield strength of the material is 1130 MPa and the ultimate tensile strength is 1161 MPa. The hardness measurement was performed for three locations on a polished plain specimen by using a Vickers hardness tester at a load of 100 gf with the load holding time of 15 s. The average hardness is 397 kgf/mm². The microstructure of the investigated material is shown in Fig. 1.

2.2. Very high cycle fatigue tests

We used an ultrasonic fatigue machine (Shimadzu USF-2000) for fatigue test. The tests are carried out with a frequency of 20 kHz at room temperature in air. The stress ratio R is -1, and a pulse of 200 ms loading with 200 ms intermittence was used. During the fatigue test, compressive cold air was used to cool down the specimens. The fatigue

specimen is an hourglass shape with the smallest diameter of 3 mm. Before fatigue test, the round notch surface was ground and polished to eliminate machine scratches.

Unless stated otherwise, all variable amplitude loadings started from the lower stress amplitude $\sigma_a^L = 450$ MPa or 430 MPa with loading cycles $n_L = 2 \times 10^6$ or $n_L = 3 \times 10^6$, and then we increased to a higher stress amplitude $\sigma_a^H = 650$ MPa with loading cycles $n_H = 4 \times 10^3$. Two specimens experienced at first a large number of variable amplitude loadings at $\sigma_a^L = 400$ MPa with $n_L = 1.5 \times 10^7$ and then $\sigma_a^H = 650$ MPa with $n_H = 1.2 \times 10^4$. This process was repeated until the specimen failed or the total cycles reached 10^9.

2.3. Observation and characterization

The fatigue-fractured surfaces of specimens were observed using a JSM-IT300 scanning electron microscope (SEM). By grinding the failed specimen with 2000 abrasive paper and employing the focused ion beam (FIB) technique, cross-section samples about 80 micros or 30 micros width along the loading direction were prepared, and the electron backscatter diffraction (EBSD) technique was used to identify the microstructure characteristic and grain refinement of the crack initiation and early growth region. The FIB was executed on the commercial crossbeam 540 FIB-SEM system by ZEISS company, and the EBSD was performed on Nordlys of Oxford Instruments. The grain boundary was analyzed by Channel 5.

Extracted cross-section samples were also prepared in some local regions by FIB technique, and were then observed by using TEM with selected area diffraction (SAD) (the diffraction area of 680 nm in diameter). The fracture surfaces of extracted samples were protected by a thin coating layer of platinum during the extraction process. The TEM was done by using JEOL 2100F. An Image-Pro Plus (IPP) version 5.0 by
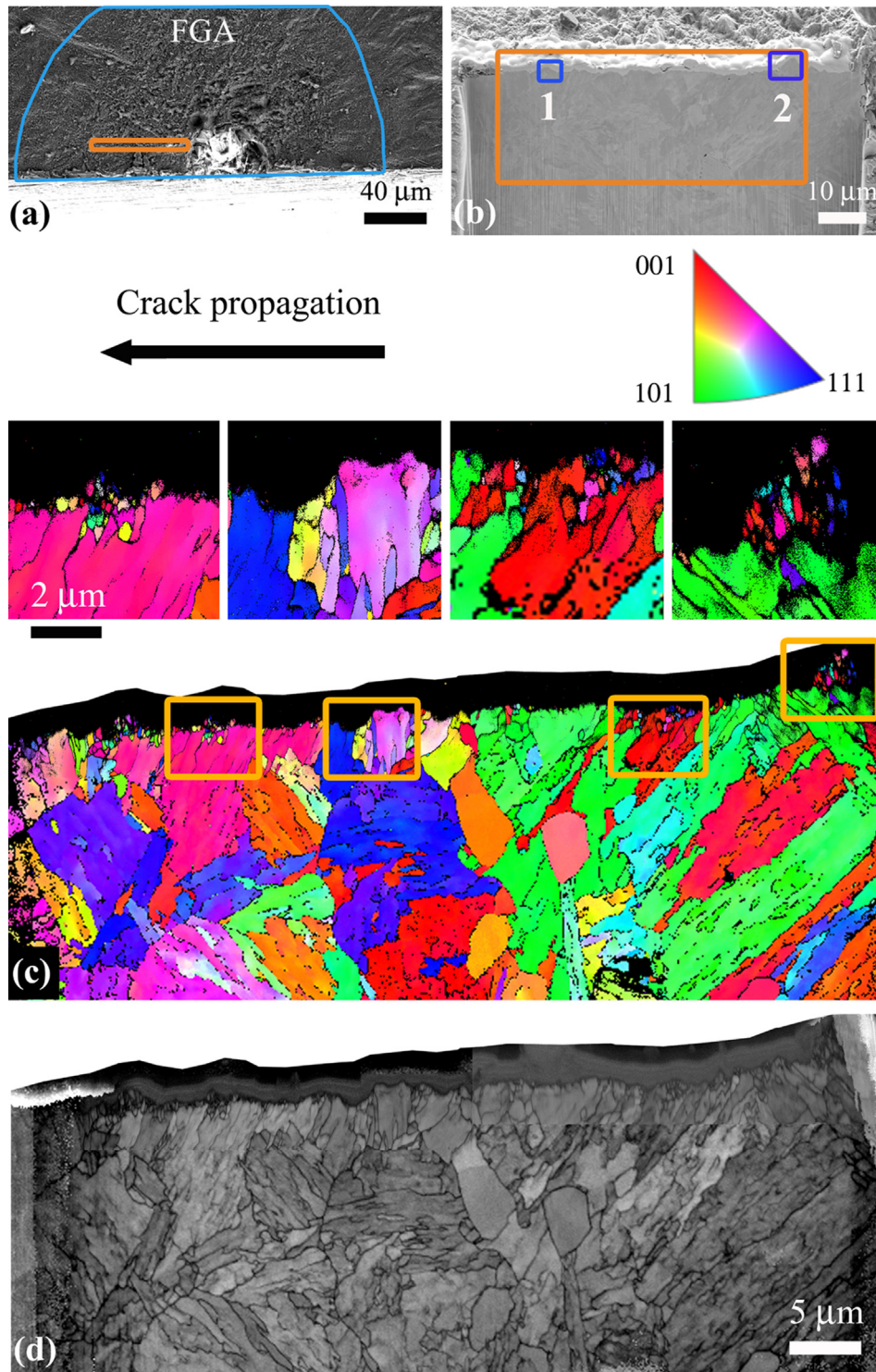
Fig. 7. Structures in the cross-section in the FGA region in the specimen failed at constant stress amplitude σ_a = 450 MPa with fatigue life of 1.174×10^8. (a), (b) SEM images for the location of the cross-section sample; (c), (d) EBSD results of the cross-section sample. The scanning step size is 20 nm for the enlarged EBSD images in orange rectangles and the upper part of the large area EBSD images in (c) and (d), and 100 nm for the lower part of the large area EBSD images in (c) and (d).

Media Cybernetics is used to measure the crack growth length due to the high and low stress sequences from the SEM images with typical "tree ring" patterns.

3. Experimental results and analyses

3.1. Fatigue data under constant amplitude loading

The S-N data under constant amplitude loading are shown in Fig. 2. It is observed that the specimens fail from the surface or interior without FGA morphology under higher stress, and tend to fail from the
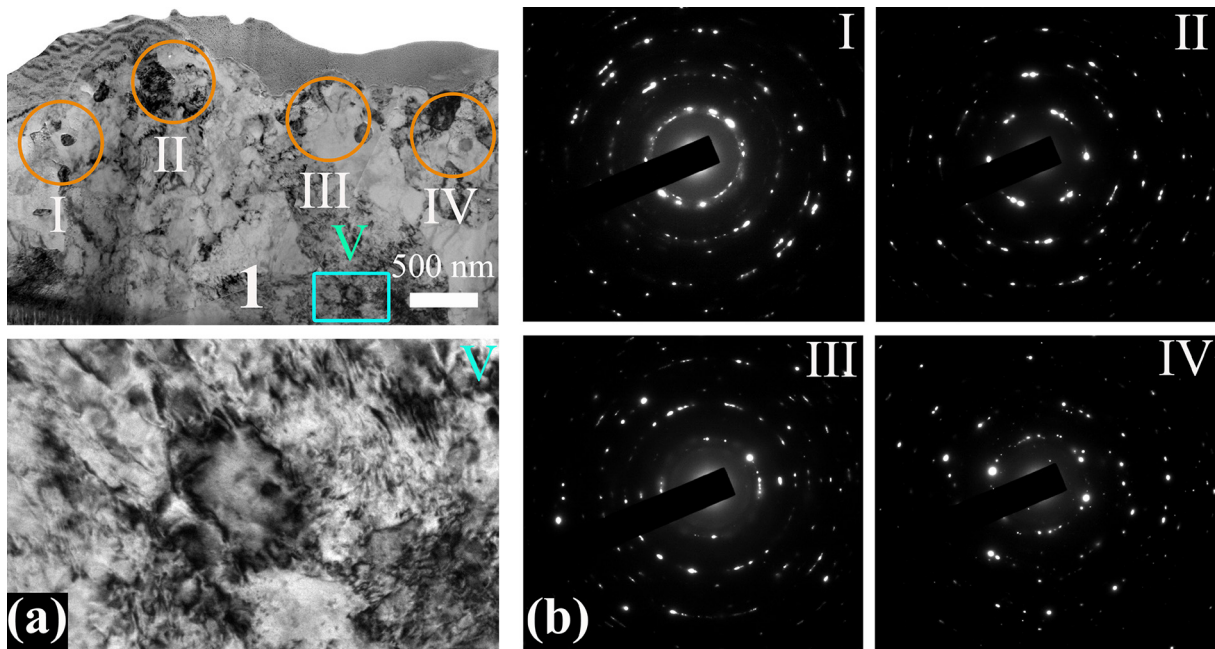
Fig. 8. TEM images of the extracted cross-section sample 1 in Fig. 7b, the circles indicate the locations where the SAD diffraction is obtained.
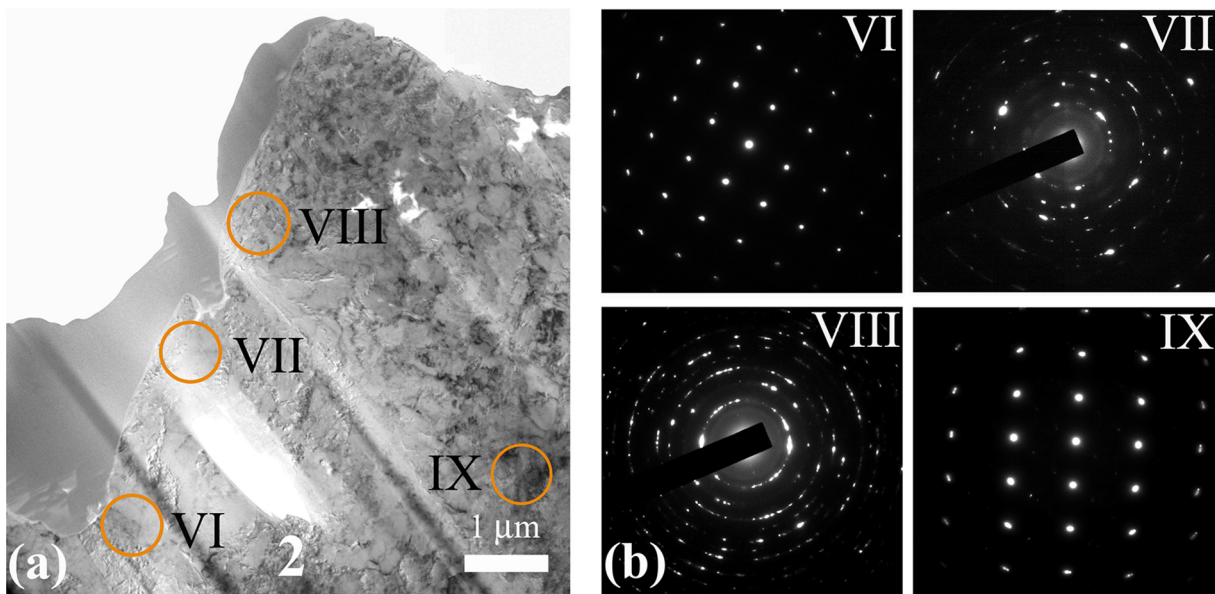

Fig. 9. TEM images of the extracted cross-section sample 2 in Fig. 7b, the circles indicate the locations where the SAD diffraction are obtained.

interior of specimens with FGA morphology under lower stress. The typical fracture morphology failed from the interior inclusion with a fish-eye pattern is shown in Fig. 3.

We also measure the inclusion size $\sqrt{area_{In}}$ and FGA size $\sqrt{area_{FGA}}$ along with the inclusion depth from the surface for specimens with interior inclusion induced fatigue failure, in which $area_{In}$ denotes the projection area of the inclusion and $area_{FGA}$ denotes the FGA area including the projection area of inclusion [8]. The relation of inclusion size and FGA size with stress amplitude is shown in Fig. 4a. The relation of inclusion depth with stress amplitude is shown in Fig. 4b. It is seen from Fig. 4 that the inclusion size is independent of the stress amplitude, while the FGA size has the decreasing trend with the increase of stress amplitude. The inclusion depth from the specimen surface tends to decrease with increasing the stress amplitude, i.e. the specimens tend to fail from the inclusions near the surface under the higher stress amplitude for the interior inclusion induced fatigue failure.

3.2. SEM observation and analyses under variable amplitude loading

Some specimens under variable amplitude loadings present clear "fatigue ring" pattern at the fracture surface, as shown in Fig. 5, which is in resemble of tree rings, and has recorded the growth history and microstructure evolution history during fatigue-crack growth. Based on the S-N curve under constant stress amplitude shown in Fig. 2, the specimens subjected to the constant stress amplitude of 650 MPa hardly form an FGA pattern. Hence, the relative rough area (i.e. the granular feature) in Fig. 5 corresponds to the sequence of cyclic loading under the low stress amplitude $\sigma_a^L = 430$ MPa, and the smooth area surrounded by two relative rough rings is the resultant of cyclic loading under the high stress amplitude $\sigma_a^H = 650$ MPa. This is in accordance with the view of fracture mechanics that the fatigue crack is retarded when the cyclic stress changes from high to low amplitude.

Based on the SEM images of typical "tree ring" pattern in the
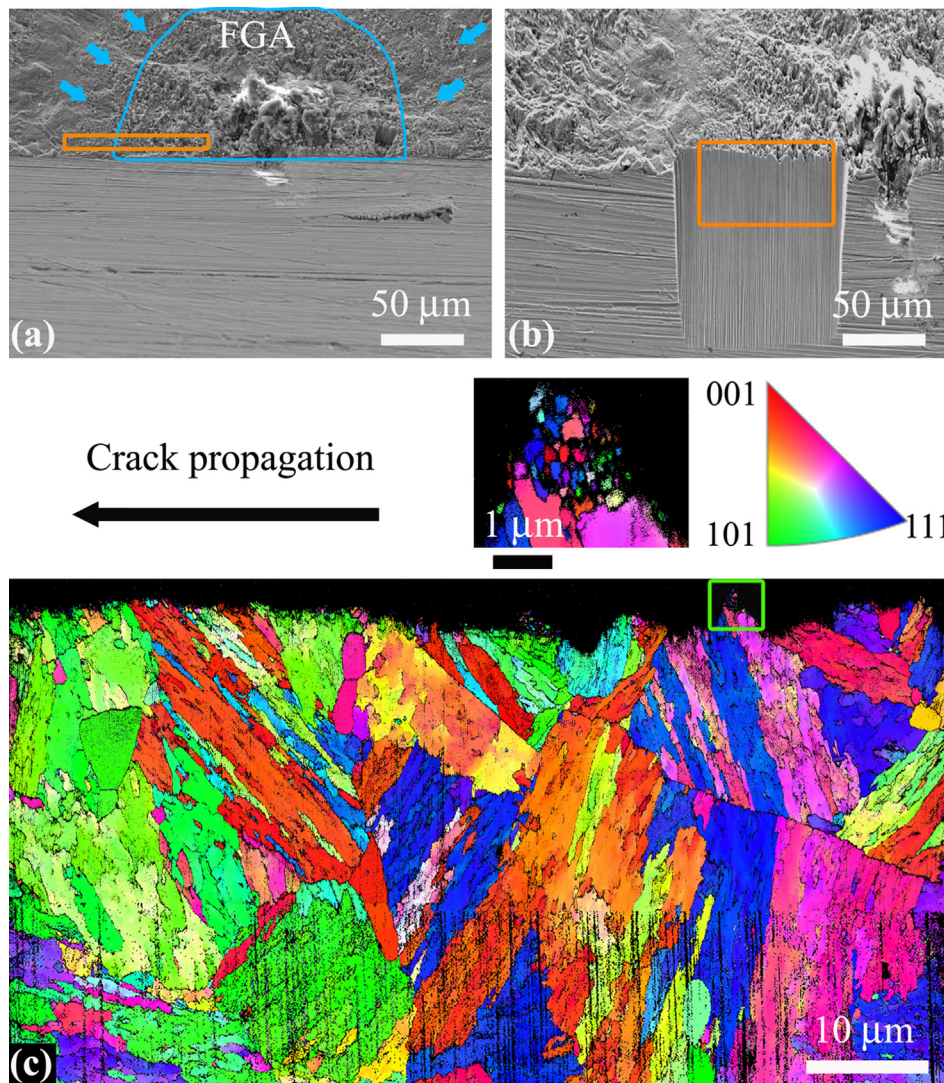
Fig. 10. Microstructures of the cross-section in the "tree ring" region for the specimen failed at a total fatigue life of 8.576×10^7 ($\sigma_a^H = 650$ MPa, $n_H = 4 \times 10^3$, $\sigma_a^L = 430$ MPa, $n_L = 3 \times 10^6$) under variable stress amplitude. (a), (b) SEM images of cross-section samples cut along the loading direction in the "tree ring" region, where the arrows point to denotes the rough area due to the low stress amplitude; (c) EBSD image for the rectangle region in (b), the scanning step is 10 nm for the enlarged EBSD image in the green rectangle, 40 nm for the upper part of the large EBSD area and 65 nm for the lower part of the large EBSD area.

fracture surface, the interior crack initiation rate is estimated and is shown in Fig. 6. The cracks after the high and low stress sequences are both approximately treated as concentric mode-I penny-shape cracks in an infinite solid under a uniform remote tensile stress, as shown in Fig. 5. For high stress, the crack growth rate da/dN and the value of ΔK are calculated by $(r_{i+1} - r_i)/n_H$ and $\Delta \sigma_a^H \sqrt{2(r_i + r_{i+1})/\pi}$, respectively, where $i = 1, 3, 5$. For low stress, they are calculated by $(r_{i+1} - r_i)/n_L$ and $\Delta \sigma_a^L \sqrt{2(r_i + r_{i+1})/\pi}$, respectively, where $i = 2, 4, 6$.

It is seen from Fig. 6 that the crack growth rate in both the rough area and the smooth area seems to be related to the stress intensity factor range, which increases with increasing the stress intensity factor range. Further, the crack propagation rate in the smooth area is larger than 10^{-10} m/cyc, but much lower in the rough area, which is smaller than one lattice spacing ($\sim 10^{-10}$ m) per cycle. This indicates that the crack growth in crack initiation stage is discrete for VHCF, i.e., the crack growth occurs first in some local regions along the crack extension direction for a number of cycles.

3.3. EBSD and TEM observation and analyses

3.3.1. Samples in FGA region under constant stress amplitude

We first examine the cross-sectional structures of samples in FGA region cut along the loading direction in the specimen under constant stress amplitude, as shown in Fig. 7. We see clearly discontinuous gradient layer structure (i.e. some regions composed of ultrafine grains and coarse grains exhibiting gradient layer characteristic of grain size, and some other regions composed of just coarse grains) in the fracture surface of crack initiation and early crack growth (i.e. FGA). The results in Fig. 7 indicate that the grain refinement does not occur in the whole FGA region, but exhibits grain level discontinuity.

The structure features in FGA are also examined by using TEM, as shown in Figs. 8 and 9. Sample 1 is tens of microns away from the inclusion, and sample 2 is close to the inclusion, as illustrated in Fig. 7b. As seen in Figs. 8 and 9, the diffused rings in locations I ~ IV of sample 1 and in locations VII and VIII of sample 2 suggest a characteristic of polycrystalline structure [28,29]. The SAD pattern with regular isolated spots in location VI of sample 2 in Fig. 9 suggests just one grain similar to the intact bulk material in location IX of sample 2. The TEM images also show that a discontinuous gradient layer structure exists in the
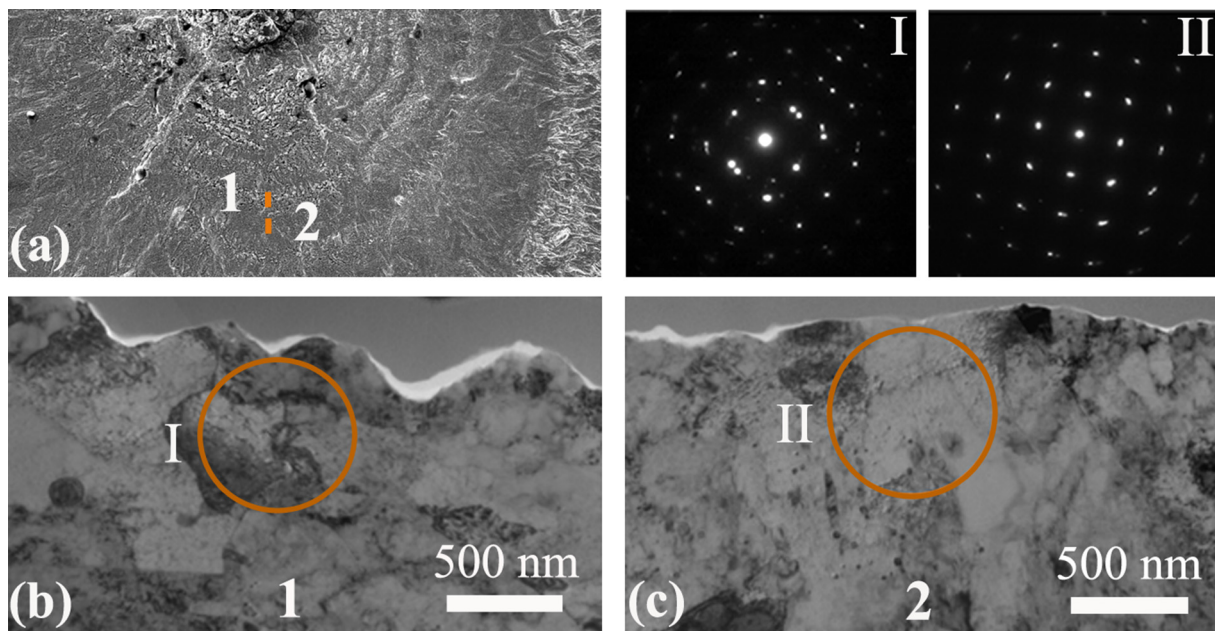
Fig. 11. SEM and TEM images of the extracted cross-section samples in the "tree ring" region for the specimen failed at a total fatigue life of 8.576×10^7 ($\sigma_a^H = 650$ MPa, $n_H = 4 \times 10^3$, $\sigma_a^L = 430$ MPa, $n_L = 3 \times 10^6$) under variable stress amplitude. (a) SEM image of the extracted cross-section locations; (b), (c) TEM images of the extracted cross-section samples 1 and 2, respectively, the circles indicate the locations where the SAD diffraction is obtained.

fracture surface of FGA, i.e. the grain refinement does not always occur beneath the rough area (FGA). In addition, a dislocation cell like structure is observed in the location V of sample 1 in Fig. 8 several microns beneath the fracture surface.

3.3.2. Samples in "tree ring" region under variable stress amplitude

We also perform the microstructure characteristics of samples in typical "tree ring" region of specimens under variable stress amplitude. The results are shown in Figs. 10–12. We see in Fig. 10 a discontinuous gradient layer in the fracture surface within the "tree ring" region which forms during crack initiation and early crack growth (i.e. FGA) stage.

Figs. 11 and 12 show the TEM images of the extracted cross-sections from specimens with typical "tree ring" patterns. Samples '1' and '4' were cut from the rough area due to the low stress amplitude while samples '2' and '3' came from the smooth area due to the high stress amplitude, as illustrated in Figs. 11a and 12a, respectively. It is seen from Fig. 11b that the SAD pattern contains isolated spots in location I in sample '1' implies the existence of a few grains within the diffraction area. While in sample '4' in Fig. 12c, the SAD patterns are composed of tiny spots forming diffusive rings in locus V and VI, which is a typical characteristic of polycrystalline structure. For sample '2' in Fig. 11c and sample '3' in Fig. 12b extracted beneath the smooth area, the SAD patterns exhibit regular isolated spots in location II while numerous tiny spots or diffused rings in location IV, which suggests coarse grain in the former region but fine polycrystalline structure in the latter region. The isolated spots or discontinuous circles in location III in Fig. 12b suggest multiple grains within the area. The TEM images also indicate that a discontinuous gradient layer structure exists beneath the fracture surface of FGA, and grain refinement does not always occur beneath the rough area (FGA).

In particular, it is found that the grain refinement could exist beneath the smooth area in some local regions under the high stress amplitude (the SAD pattern in location IV of sample 3 in Fig. 12b). It is thought that, in the crack initiation and early growth stage, the grain refinement occurs in some local regions under the low stress amplitude for a number of cyclic loadings before the micro crack formation or crack extension. Then, the relative larger crack driving force due to the

following high stress amplitude promotes the crack growth and results in the smooth morphology.

3.3.3. Samples in a secondary crack initiation region

We now examine the cross-sectional microstructure in samples cut along the loading direction nearby the secondary crack. The SEM and EBSD images of the samples are shown in Fig. 13. The misorientation angle used for the determination of grain boundaries is 10 degree. Black profiles between grains represent grain boundaries. Fig. 13a shows how the samples '1' and '2' of our interest are cut. The SEM images of the two samples are shown in Fig. 13b and 13c, respectively. The discontinuous gradient layer shown in Fig. 13d (region II) suggests its formation in the crack initiation and early growth stage rather than after the formation of the primary fatigue crack, which could initiate the crack within the refined grains (e.g. left parts of region I in Fig. 13d and region III in Fig. 13e) or along the boundaries of the refined grains and the coarse grains (e.g. right parts of region I in Fig. 13d and region III in Fig. 13e). A comparison between Fig. 13b and d with Fig. 13c and e indicates that the crack growth may occur first in some local weak regions by the formation of micro cracks and then coalesce in the vicinity of the primary crack during cyclic loadings.

The EBSD and TEM microstructures of the samples parallel to the loading direction in the specimen under constant and variable amplitude loadings confirm this discontinuous gradient layer characteristic beneath the fracture surface of FGA. We examine closely the composition of those refined grains using electron energy loss spectroscopy for TEM for elemental composition analysis and confirm that the fine grain is a resultant of deformation other than oxidation.

The present results differ from the existing understanding regarding the characteristic of rough area region (FGA). For the compression induced grain refinement model, the microstructure beneath FGA is a thin layer of nanograins [28,29]. In addition, grains in the two sides of the crack would have equal chance for grain refinement. That is not the case we see in Fig. 13d and e. Indeed, Sakai et al. [27] observed that the fine grain microstructure was only at one side of the mated fracture surfaces beneath the FGA. Sander et al. [30] reported no FGA visible on the fracture surface for a high strength 34CrNiMo6 steel in VHCF regime. All these results along with the present observations suggest that
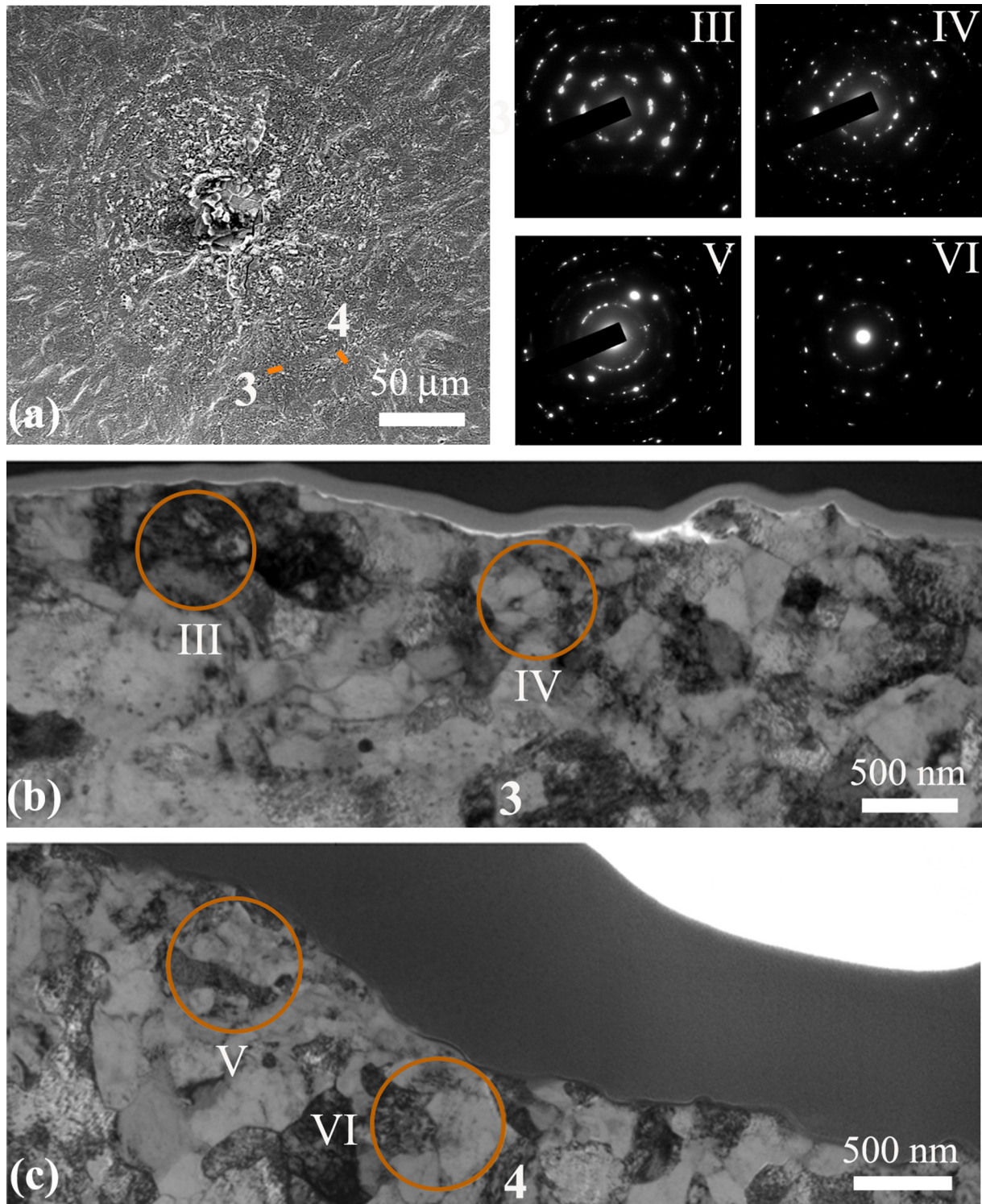
Fig. 12. SEM and TEM images of the extracted cross-section samples in the "tree ring" region for the specimen failed at a total fatigue life of 7.0608×10^7 ($\sigma_a^H = 650$ MPa, $n_H = 4 \times 10^3$, $\sigma_a^L = 450$ MPa, $n_L = 2 \times 10^6$) under variable stress amplitude. (a) SEM image of the extracted cross-section locations; (b), (c) TEM images of the extracted cross-section samples 3 and 4, respectively, the circles indicate the locations where the SAD diffraction is obtained.

the crack initiation and early growth region for VHCF of high strength steels could present FGA (rough area) morphology or no FGA, which is greatly influenced by the loading condition and the microstructure characteristics. Moreover, the grain refinement does not always occur for the microstructure beneath FGA.

4. Discussion

The present EBSD and TEM observations indicate that a gradient structure of grain size forms in some local regions ahead of the crack tip during the crack initiation and early growth stage. According to the work by Van Swam et al. [31], the microstructure evolved through a rearrangement of dislocations in clearly defined dislocation cells for
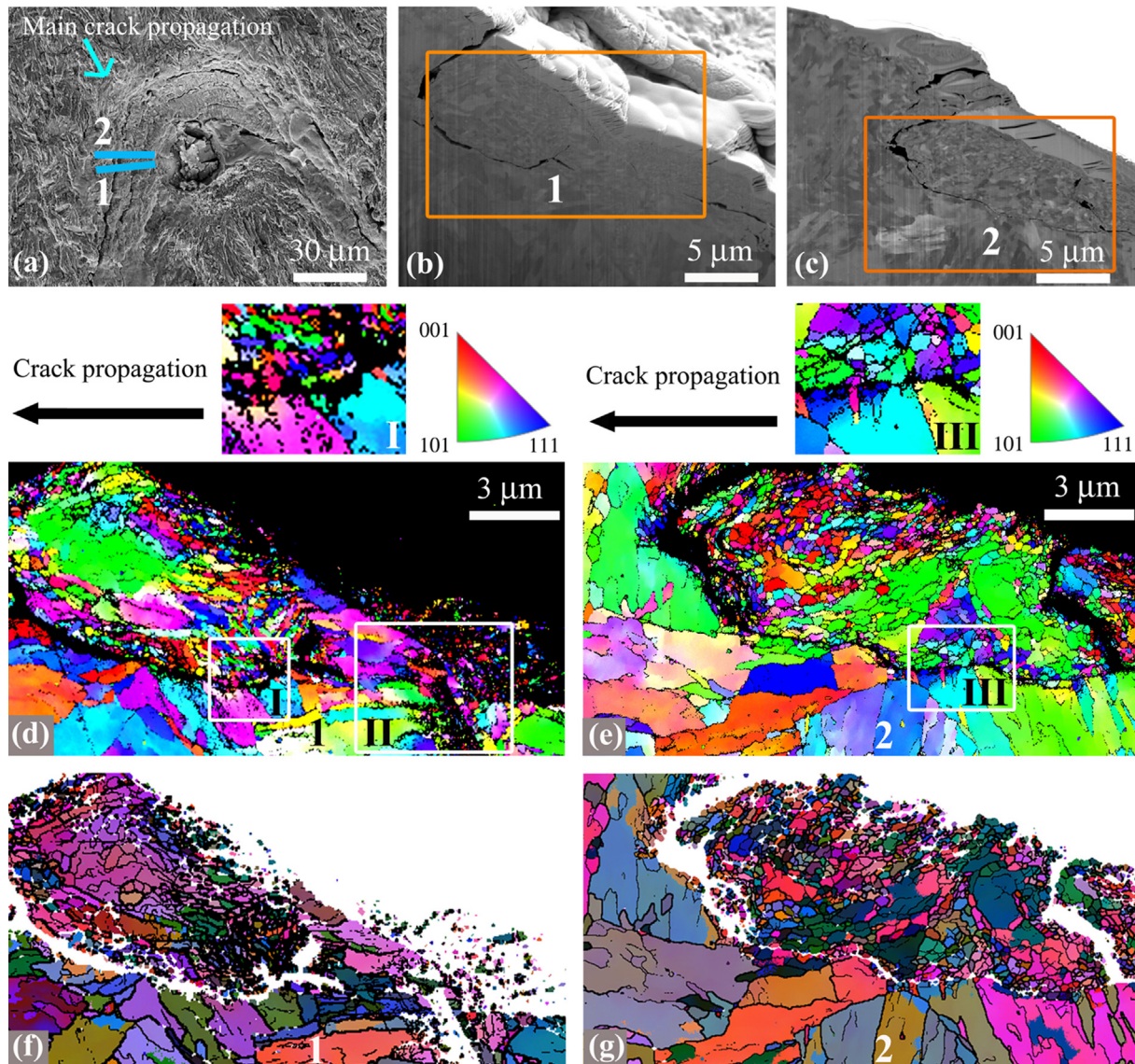
Fig. 13. Cross-sectional microstructure in samples for a secondary crack initiation region (parts of the crack surface is beneath the final fracture crack surface) subjected to a total cyclic loading of 1.3913×10^7 ($\sigma_a^H = 650$ MPa, $n_H = 4 \times 10^3$, $\sigma_a^L = 450$ MPa, $n_L = 2 \times 10^6$) after a number of 1.501×10^8 cycles ($\sigma_a^H = 650$ MPa, $n_H = 1.2 \times 10^4$, $\sigma_a^L = 400$ MPa, $n_L = 1.5 \times 10^7$). (a)-(c) SEM images of cross-section samples cut along the loading direction in the crack initiation and early growth region. (d) and (e) EBSD inverse pole figure maps for samples 1 and 2 in (b) and (c), respectively; (f) and (g) EBSD grain boundary maps for samples 1 and 2 in (b) and (c), respectively, in which the thin black line denotes the low angle grain boundaries (2–10°), the bold black line denotes the high angle grain boundaries (> 10°); The scanning step size is 40 nm for the EBSD images in (d) and (f), and 25 nm for the EBSD images in (e) and (g).

martensitic steels during cyclic deformation. The dislocation cell structure was also observed in the ferrite grains in VHCF regime, which led to the formation of small sub grains or low angle grain boundaries [32]. These results indicate that the grain refinement could occur in the crack initiation region before the formation of micro cracks. For the present test material, the dislocation cell like structure is observed in the location several microns beneath the fracture surface (location V in Fig. 8a), and the grain refinement is also observed in the vicinity of initiated crack in the crack initiation region (right parts of region II in Fig. 13d). Therefore, it is considered that the gradient layer (i.e. grain refinement) is caused by the interaction between the dislocations in the vicinity of crack origin or initiated crack tip due to local high stress [33]. The micro crack forms within the refined grains [29,34] due to the decrease of threshold value for crack initiation in regions of fine grains [35], or along the fine grain – coarse grain interface. The first case would lead to the observation of fine grains in the mated fracture surfaces; and the second case would give rise to observation of fine

grains only in one side of the fracture surface. We have seen these two cases in Fig. 13d and e. The gradient layer due to the cyclic loadings induces the local decrease of threshold value of crack initiation in refined grains, which promotes the formation of micro crack and the crack initiation.

The cyclic plastic deformation in the materials is highly localized in the VHCF regime or the elastic deformation regime [36]. This high strain localization leads to the accumulation of irreversible plastic deformation followed by small crack nuclei that initiates at the interface of inclusion and matrix, the inclusion, interior of grain, the phase or grain boundaries [37,38]. This indicates that the micro crack may form at first in some local regions before the formation of grain refinement during the cyclic loadings, which is supported by the observation of FGA formation surrounding the internal grain boundary for high strength steels in VHCF regime [39]. In this scenario, there is no gradient layer structure (i.e. grain refinement) formation alongside the crack surface. Whether the gradient layer structure forms or not

depends not only the loading conditions but also the materials themselves especially the local microstructure around a formed crack. This could also explain why there are no refined grains observed in the crack initiation region in some cases in high strength steels failed in VHCF regime even though the rough morphology (FGA) is presented in the fracture surface [39].

We also perform a series of finite element simulations for the strain field along the crack surface and at the crack tip for the interior penny cracks with different diameters (100 μm, 200 μm and 300 μm) by combining the nonlinear Armstrong-Frederick kinematic hardening law [40] and the isotropic hardening law in the commercial FEM package ABAQUS [41]. The applied maximum stresses are 430 MPa and 650 MPa, respectively, and the stress ratio R is −1, based on the variable loading condition. Simulation results reveal that the crack tip could be deformed plastically [42] but the crack surface does not deform plastically, indicating that the grain refinement forms before the formation of crack surface if there is grain refinement in FGA.

5. Conclusions

We investigates the mechanism of crack initiation and early growth of high strength steels in VHCF regime by constant and specially designed variable amplitude loadings. We observe discontinuous gradient region in the crack initiation and early growth stage. Whether the gradient layer structure (i.e. grain refinement) forms or not depends not only the loading condition but also the materials themselves especially the local microstructure around formed crack or crack origin. The crack extension in the crack initiation and early growth stage is far below one lattice spacing ($\sim 10^{-10}$ m) per cycle. The equivalent crack growth rate is in the magnitude of 10^{-12}–10^{-11} m/cyc. We propose that the crack initiation and early growth is the result of formation of gradient layer structure caused by the interaction between the dislocations in the vicinity of crack origin or crack tip over a number of cyclic loadings followed by micro cracks, in combination with the formation of the micro cracks before the formation of gradient layer structure in some regions during this process. The present observations and results are vital for understanding the mechanism of crack initiation and early growth for high strength steels in VHCF regime.

Acknowledgements

References

[1] Koyama M, Zhang Z, Wang MM, Ponge D, Raabe D, Tsuzaki T, et al. Bone-like crack resistance in hierarchical metastable nanolaminate steels. Science 2017;355:1055–7.

[2] Pan QS, Zhou HF, Lu QH, Gao HJ, Lu L. History-independent cyclic response of nanotwinned metals. Nature 2017;551:214–7.

[3] Zhu ML, Jin L, Xuan FZ. Fatigue life and mechanistic modeling of interior micro-defect induced cracking in high cycle and very high cycle regimes. Acta Mater 2018;157:259–75.

[4] Karakoc O, Hayrettin C, Canadinc D, Karaman I. Role of applied stress level on the actuation fatigue behavior of NiTiHf high temperature shape memory alloys. Acta Mater 2018;153:156–68.

[5] Li LL, Zhang ZJ, Zhang P, Wang ZG, Zhang ZF. Controllable fatigue cracking mechanisms of copper bicrystals with a coherent twin boundary. Nat Commun 2014;5:3536.

[6] Song M, Du K, Huang ZY, Huang H, Nie ZR, Ye HQ. Deformation-induced dissolution and growth of precipitates in an Al–Mg–Er alloy during high-cycle fatigue. Acta Mater 2014;81:409–19.

[7] Chandran KSR. Duality of fatigue failures of materials caused by Poisson defect

[8] statistics of competing failure modes. Nat Mater 2005;4:303–8.

[8] Murakami Y, Nomoto T, Ueda T. Factors influencing the mechanism of superlong fatigue failure in steels. Fatigue Fract Eng Mater Struct 1999;22:581–90.

[9] Wu SC, Liu YX, Li CH, Kang GZ, Liang SL. On the fatigue performance and residual life of intercity railway axles with inside axle boxes. Eng Fract Mech 2018;197:176–91.

[10] Gupta S, Barrios A, England No, Pierron ON. Improved very high cycle bending fatigue behavior of Ni microbeams with Au coatings. Acta Mater 2018;161:444–55.

[11] Qian G, Zhou C, Hong Y. Experimental and theoretical investigation of environmental media on very-high-cycle fatigue behavior for a structural steel. Acta Mater 2011;59:1321–7.

[12] Sun C, Lei Z, Xie J, Hong Y. Effects of inclusion size and stress ratio on fatigue strength for high-strength steels with fish-eye mode failure. Int J Fatigue 2013;48:19–27.

[13] Wang XG, Feng ES, Jiang C. A microplasticity evaluation method in very high cycle fatigue. Int J Fatigue 2017;94:6–15.

[14] Naito T, Ueda H, Kikuchi M. Fatigue behavior of carburized steel with internal oxides and non-martensitic microstructure near the surface. Metall Trans A 1984;15:1431–6.

[15] Wang QY, Berard JY, Dubarre A, Baudry G, Rathery S, Bathias C. Gigacycle fatigue of ferrous alloys. Fatigue Fract Eng Mater Struct 1999;22:667–72.

[16] Yang Z, Li S, Liu Y, Li G, Hui W, Weng Y. Estimation of the size of GBF area on fracture surface for high strength steels in very high cycle fatigue regime. Int J Fatigue 2008;30:1016–23.

[17] Huang Z, Wagner D, Bathias C, Paris PC. Subsurface crack initiation and propagation mechanisms in gigacycle fatigue. Acta Mater 2010;58:6046–54.

[18] Mughrabi H. Microstructural mechanisms of cyclic deformation, fatigue, crack initiation, and early crack growth. Philos Trans A Math Phys Eng Sci 2015;373:1–21.

[19] Sun C, Song Q, Hu Y, Wei Y. Effects of intermittent loading on fatigue life of a high strength steel in very high cycle fatigue regime. Int J Fatigue 2018;117:9–12.

[20] Murakami Y. Metal fatigue: effects of small defects and nonmetallic inclusions. Oxford: Elsevier Book; 2002.

[21] Sakai T, Sato Y. Characteristics S-N properties of high carbon chromium bearing steel under axial loading in long life fatigue. Fatigue Fract Eng Mater Struct 2002;25:765–73.

[22] Ochi Y, Matsumura T. High-cycle rotating bending fatigue property in very long-life regime of high-strength steels. Fatigue Fract Eng Mater Struct 2002;25:823–30.

[23] Shiozawa K, Morii Y, Nishino S, Lu L. Subsurface crack initiation and propagation mechanism in high strength steel in a very high cycle fatigue regime. Int J Fatigue 2006;28:1521–32.

[24] Nakamura T, Oguma H, Shinohara Y. The effect of vacuum-like environment inside sub-surface fatigue crack on the formation of ODA fracture surface in high strength steel. Procedia Eng 2010;2:2121–9.

[25] Ogawa T, Stanzl-Tschegg SE, Schönbauer BM. A fracture mechanics approach to interior fatigue crack growth in the very high cycle regime. Eng Fract Mech 2014;115:241–54.

[26] Grad P, Reuscher B, Brodyanski A. Mechanism of fatigue crack initiation and propagation in the very high cycle fatigue regime of high-strength steels. Scr Mater 2012;67:838–41.

[27] Sakai T, Oguma N, Morikawa A. Microscopic and nanoscopic observations of metallurgical structures around inclusions at interior crack initiation site for a bearing steel in very high-cycle fatigue. Fatigue Fract Eng Mater Struct 2015;38:1305–14.

[28] Hong Y, Liu X, Lei Z, Sun C. The formation mechanism of characteristic region at crack initiation for very-high-cycle fatigue of high-strength steels. Int J Fatigue 2016;89:108–18.

[29] Tofique MW, Bergström J, Svensson K. Very high cycle fatigue of cold rolled stainless steels, crack initiation and formation of the fine granular area. Int J Fatigue 2017;100:238–50.

[30] Sander M, Müller T, Lebahn J. Influence of mean stress and variable amplitude loading on the fatigue behaviour of a high-strength steel in VHCF regime. Int J Fatigue 2014;62:10–20.

[31] Van Swam LF, Pelloux RM. Fatigue behavior of maraging steel 300. Metall Trans A 1975;6:45–54.

[32] Koster M, Wagner G, Eifler D. Cyclic deformation behavior of a medium carbon steel in the VHCF regime. Procedia Eng 2010;2:2189–97.

[33] Chai G, Forsman T, Gustavsson F. Microscopic and nanoscopic study on subsurface damage and fatigue crack initiation during very high cycle fatigue. Int J Fatigue 2016;83:282–92.

[34] Spriestersbach D, Brodyanski A, Lösch J, Kopnarski M, Kerscher E. Very high cycle fatigue of bearing steels with artificial defects. Proc Struct Integr 2016;2:1101–8.

[35] Niendorf T, Rubitschek F, Maier HJ, Canadine D, Karaman I. On the fatigue crack growth–microstructure relationship in ultrafine-grained interstitial-free steel. J Mater Sci 2010;45:4813–21.

[36] Chai G, Zhou N, Ciurea S, Andersson M, Peng RL. Local plasticity exhaustion in a very high cycle fatigue regime. Scr Mater 2012;66:769–72.

[37] Bach J, Möller JJ, Göken M, Bitzek E, Höppel HW. On the transition from plastic deformation to crack initiation in the high- and very high-cycle fatigue regimes in plain carbon steels. Int J Fatigue 2016;93:281–91.

[38] Torabian N, Favier V, Dirrenberger J, Adamski F, Ziaei-Rad S, Ranc N. Correlation of the high and very high cycle fatigue response of ferrite based steels with strain rate-temperature conditions. Acta Mater 2017;134:40–52.

[39] Jiang Q, Sun C, Liu X, Hong Y. Very-high-cycle fatigue behavior of a structural steel with and without induced surface defects. Int J Fatigue 2016;93:352–62.

[40] Armstrong PJ, Frederick CO. A mathematical representation of the multiaxial bauschinger effect. CEGB Report No. RD/B/N731; 1966.

[41] Hibbitt, Karlsson, and Sorensen. ABAQUS Version 5.7; 1997.

[42] Mughrabi H. Cyclic slip irreversibility and fatigue life: A microstructure-based analysis. Acta Mater 2013;61:1197–203.